

Controllable Multi-Wave Mixing Talbot Effect

Yiqi Zhang, Xin Yao, Chenzhi Yuan, Peiying Li, Jiamin Yuan,
Weikang Feng, Shuqiao Jia, and Yanpeng Zhang*

*Key Laboratory for Physical Electronics and Devices of the Ministry of Education &
Shaanxi Key Lab of Information Photonic Technique,
Xi'an Jiaotong University, Xi'an 710049, China*

*corresponding author: ypzhang@mail.xjtu.edu.cn

Abstract

We theoretically study the Talbot effects resulted from the four-wave mixing and six-wave mixing signals, which are periodically modulated due to the coherence control effect. Corresponding to different dressing states, the enhancement and suppression conditions, that will affect the properties of the multi-wave mixing signals are also discussed in detail. Such proposal can be useful in all optical-controlled pattern formation and propagation of light.

1 Introduction

Talbot effect, which was observed by H. F. Talbot in 1836 [1] and first analytically explained by Lord Rayleigh in 1881 [2], is a near-field diffraction phenomenon that the light field spatially imprinted with periodic structure can have self-imaging at certain periodic imaging planes (the so-called Talbot planes). Such self-imaging effect holds a range of applications from image preprocessing and synthesis, photolithography, optical testing, optical metrology, spectrometry, to optical computing [3].

To date, studies on Talbot effect have been reported associated with atomic waves [4, 5], surface waves [6, 7], nonclassical light [8], or waveguide arrays [9]. Among the quiverful of researches, the nonlinear Talbot effect with second-harmonic (SH) were demonstrated both experimentally [10] and theoretically [11] in periodically poled LiTaO₃ (PPLT) crystal for the first time. The Talbot effect with beam imprinted with an electromagnetically induced grating (EIG) has been also proposed [12]. However, no progress in higher nonlinear optical process was reported before as far as to our knowledge.

The crucial point and the guiding ideology to observe the Talbot effect is how to produce a spatial periodical incidence in transverse dimension. From this point of view, it is natural to realize that researchers have created spatially periodic four-wave mixing (FWM) and six-wave mixing (SWM) signals due to the periodic atomic coherence induced by standing waves (SWs) [13–16], which can play an important role in lasing without inversion [17], slow light generation [18], photon controlling and information storage [19–21], fiber lasers [22, 23], and so on. The periodic pattern of the multi-wave mixing (MWM) signals can be flexibly controllable by adjusting the atomic coherence via changing the beam detunings.

In this article, we investigate the MWM Talbot effect for the first time. And as the coexisting FWM and SWM processes have been observed in the Cd (S, Se) semiconductor doped glasses [24], the idea can be also executed in some solid crystals such as Pr-doped YSO crystals [24–27] besides atomic vapors. The article is organized as follows: in Sec. 2, we introduce the basic theory includes the energy level systems, some conceptions, and how to prepare the periodic FWM and MWM signals; in Sec. 3, we discuss the enhancement and suppression conditions, due to which the energy levels split; in Sec. 4, we investigate the Talbot effects of the periodic MWM signals; and in the last section, we conclude the article.

2 Theoretical Model and Analysis

We consider the FWM and SWM processes in the reverse Y-type atomic levels system derived by five beams, as shown in Figs. 1(a) and (b). A candidate for the systems are rubidium atomic vapors. Also, in Pr:YSO crystal, the energy-level system with $|0\rangle = |^3H_4(\pm 3/2)\rangle$, $|1\rangle = |^1D_2(\pm 3/2)\rangle$, $|3\rangle = |^3H_4(\pm 1/2)\rangle$ can be used as a sub-system of our proposed system. Here we note that to guarantee the applicability of our proposal to all the possible candidate

systems, we choose parameters in simulation arbitrarily. Figs. 1(c) and (d) are the corresponding beam geometric configurations. The transition $|0\rangle \rightarrow |1\rangle$ with resonant frequency Ω_{10} is probed by beam \mathbf{E}_1 (with frequency ω_1 , frequency detuning Δ_1 and wave-vector \mathbf{k}_1); $|1\rangle \rightarrow |2\rangle$ with resonant frequency Ω_{21} is pumped by beams \mathbf{E}_2 (with ω_2 , Δ_2 and \mathbf{k}_2) and \mathbf{E}'_2 (with ω_2 , Δ_2 and \mathbf{k}'_2); $|3\rangle \rightarrow |1\rangle$ with resonant frequency Ω_{31} is pumped by beams \mathbf{E}_3 (with ω_3 , Δ_3 and \mathbf{k}_3) and \mathbf{E}'_3 (with ω_3 , Δ_3 and \mathbf{k}'_3). The frequency detunings are defined as $\Delta_1 = \Omega_{10} - \omega_1$, $\Delta_2 = \Omega_{21} - \omega_2$, and $\Delta_3 = \Omega_{13} - \omega_3$. In the Cartesian coordinate introduced in Figs. 1(c) and (d), the wave-vectors are elaborated designed that \mathbf{E}_1 propagates z -negative with an angle θ_1 ; \mathbf{E}_2 and \mathbf{E}_3 propagate along the opposite direction of \mathbf{k}_1 , deviating from the z -positive direction with θ_1 ; \mathbf{E}'_2 and \mathbf{E}'_3 propagate symmetrically to \mathbf{E}_2 and \mathbf{E}_3 with respect to z -negative direction.

As shown in Fig. 1(a), if the fields \mathbf{E}_2 , \mathbf{E}'_2 , \mathbf{E}_3 and \mathbf{E}'_3 are not strong sufficiently, we consider the undressed FWM signal \mathbf{E}_F with $\omega_F = \omega_1$ and $\mathbf{k}_F = \mathbf{k}_1 + \mathbf{k}_3 - \mathbf{k}'_3$; if \mathbf{E}_3 and \mathbf{E}'_3 are weak but \mathbf{E}_2 and \mathbf{E}'_2 are strong sufficiently to induce dressing effect (act as the dressing fields), we consider the singly-dressed FWM signal \mathbf{E}_{F1} with $\omega_{F1} = \omega_1$ and $\mathbf{k}_{F1} = \mathbf{k}_F$. While if \mathbf{E}_3 and \mathbf{E}'_3 are also strong sufficiently to induce dressing effect, we consider the doubly-dressed FWM signal \mathbf{E}_{F2} with $\omega_{F2} = \omega_1$ and $\mathbf{k}_{F2} = \mathbf{k}_F$. Even though \mathbf{E}_2 and \mathbf{E}'_2 will induce another FWM signal (P polarization), we still can get the expected FWM signal via a polaroid for its polarization selectivity. By using five beams with polarizations as shown in Fig. 1(b), a SWM signal \mathbf{E}_S with $\omega_S = \omega_1$ and $\mathbf{k}_S = \mathbf{k}_1 + \mathbf{k}_2 - \mathbf{k}'_2 + \mathbf{k}_3 - \mathbf{k}'_3$ can be obtained.

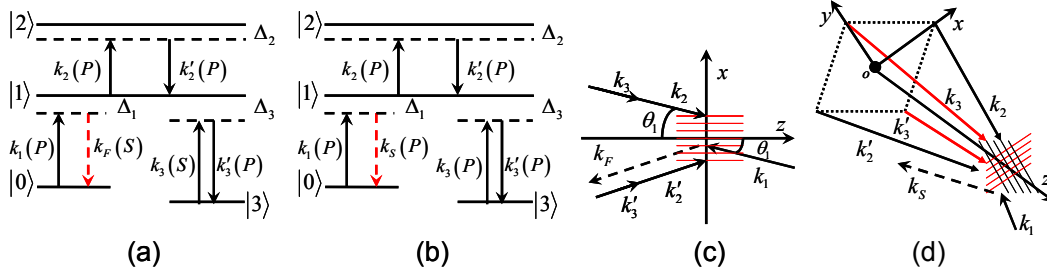


Figure 1: The schematic of the reverse Y-type atomic system to produce MWM signals. (a) \mathbf{k}_F represents the singly- or doubly-dressed FWM corresponds to a weak or strong \mathbf{k}_3 , respectively. (b) Emission of the doubly-dressed SWM signal \mathbf{k}_S . The letters S and P in the brackets mean the polarization of the wave. (c) and (d) The Cartesian geometric configurations to generate FWM and SWM signals, respectively; The SWs along x and y are constructed by \mathbf{k}_2 , \mathbf{k}'_2 and \mathbf{k}_3 , \mathbf{k}'_3 , respectively.

To obtain the MWM signal, we solve the density matrix equations and the Liouville pathways for $\rho_{10}^{(3)}$ and $\rho_{10}^{(5)}$, the amplitude of which is proportional to that of the MWM signal. First, for the undressed FWM signal \mathbf{E}_F , we can obtain $\rho_{10}^{(3)}$ via the Liouville pathway [28] as

$$\rho_{00}^{(0)} \xrightarrow{\mathbf{E}_1} \rho_{10}^{(1)} \xrightarrow{(\mathbf{E}_3)^*} \rho_{30}^{(2)} \xrightarrow{\mathbf{E}'_3} \rho_{10}^{(3)}, \quad (1)$$

$$\rho_{10}^{(3)} = \frac{-iG_{\text{FWM}}}{d_1^2 d_3}, \quad (2)$$

where $G_{\text{FWM}} = G_{10}G_{30}(G'_{30})^* \exp(i\mathbf{k}_F \cdot \mathbf{r}) \exp(-i\omega_1 t)$, $d_1 = \Gamma_{10} + i\Delta_1$, $d_3 = \Gamma_{30} + i(\Delta_1 - \Delta_3)$. The terms $G_{i0} = \mu_{mn}E_{i0}/\hbar$ and $G'_{i0} = \mu_{mn}E'_{i0}/\hbar$ with $i = 1, 2$ are the amplitudes of the Rabi frequencies of \mathbf{E}_i and \mathbf{E}'_i , respectively, where μ_{mn} is the dipole moment of transition between $|m\rangle$ and $|n\rangle$, which is driven by \mathbf{E}_i ; E_{i0} and E'_{i0} are the amplitudes of \mathbf{E}_i and \mathbf{E}'_i , respectively. Γ_{pq} represents the transverse relaxation rate between $|p\rangle$ and $|q\rangle$ for $p \neq q$, and the longitudinal relaxation rate of $|p\rangle$ for $p = q$. It is obvious to see that the amplitude of $\rho_{10}^{(3)}$ in Eq. (2) is spatial independent, so \mathbf{E}_F is uniform.

Next, we consider the singly-dressed FWM process from \mathbf{E}_2 and \mathbf{E}'_2 , which are strong sufficiently. In the spatial interaction region, \mathbf{E}_2 and \mathbf{E}'_2 will interfere with each other and create a SW, which leads to periodic Rabi frequency amplitude $|G_{2t}(x)|^2 = G_{20}^2 + G_{20}'^2 + 2G_{20}G_{20}' \cos[2(k_2 \sin \theta_1)x]$. Therefore, the Liouville pathway for \mathbf{E}_{F1} will be modified into:

$$\rho_{00}^{(0)} \xrightarrow{\mathbf{E}_1} \rho_{|G_{2t}(x)\pm 0}^{(1)} \xrightarrow{(\mathbf{E}_3)^*} \rho_{30}^{(2)} \xrightarrow{\mathbf{E}'_3} \rho_{|G_{2t}(x)\pm 0}^{(3)}, \quad (3)$$

where $|G_{2t}(x)\pm\rangle$ represent two dressed states produced by the spatial periodic dressing effect. According to Eq.

(3), we can obtain the spatial-dependent dressed density matrix element as:

$$\rho_{F1}^{(3)}(x) = \frac{-iG_{\text{FWM}}}{[d_1 + |G_{2t}(x)|^2/d_2]^2 d_3}, \quad (4)$$

where $d_2 = \Gamma_{20} + i(\Delta_1 + \Delta_2)$. The amplitude of $\rho_{F1}^{(3)}$ shows obvious periodic variation along x direction with a period of $d_x = \lambda_2/(2\sin\theta_1)$.

When \mathbf{E}_3 and \mathbf{E}'_3 get strong significantly, we will get the doubly-dressed FWM signal \mathbf{E}_{F2} . The Liouville pathway and the doubly-dressed density matrix element for this case are

$$\rho_{00}^{(0)} \xrightarrow{\mathbf{E}_1} \rho_{|G_{3t} \pm G_{2t}(x) \pm 0}^{(1)} \xrightarrow{(\mathbf{E}_3)^*} \rho_{30}^{(2)} \xrightarrow{\mathbf{E}'_3} \rho_{|G_{3t} \pm G_{2t}(x) \pm 0}^{(3)}, \quad (5)$$

$$\rho_{F2}^{(3)}(x) = \frac{-iG_{\text{FWM}}}{[d_1 + |G_{30}|^2/d_3 + |G_{2t}(x)|^2/d_2]^2 d_3}. \quad (6)$$

In Fig. 1(b), the spatially periodic dressing effect from \mathbf{E}_2 and \mathbf{E}'_2 remains, and the dressing fields \mathbf{E}_3 and \mathbf{E}'_3 with same polarization (compared to the case of Eq. (6) with \mathbf{E}_3 and \mathbf{E}'_3 having orthogonal polarizations) can also interfere with each other and create periodic Rabi frequency amplitude $|G_{3t}(y)|^2 = G_{30}^2 + G_{30}'^2 + 2G_{30}G_{30}'\cos[2(k_3\sin\theta_2)y]$. Therefore, this SWM will suffer from two dressing effects, which are both spatial periodic with different periods d_x and $d_y = \lambda_3/(2\sin\theta_2)$, respectively. The corresponding Liouville pathway and doubly-dressed density matrix element are

$$\rho_{00}^{(0)} \xrightarrow{\mathbf{E}_1} \rho_{|G_{3t}(y) \pm G_{2t}(x) \pm 0}^{(1)} \xrightarrow{(\mathbf{E}_3)^*} \rho_{30}^{(2)} \xrightarrow{\mathbf{E}'_3} \rho_{|G_{3t}(y) \pm G_{2t}(x) \pm 0}^{(3)} \xrightarrow{(\mathbf{E}_2)^*} \rho_{2\pm 0}^{(4)} \xrightarrow{\mathbf{E}'_2} \rho_{|G_{3t}(y) \pm G_{2t}(x) \pm 0}^{(5)}, \quad (7)$$

$$\rho_{10}^{(5)} = \frac{iG_{\text{SWM}}}{[d_1 + |G_{2t}(x)|^2/d_2 + |G_{3t}(y)|^2/d_3]^3 d_2 d_3}, \quad (8)$$

where $G_{\text{SWM}} = G_{10}G_{20}(G'_{20})^*G_{30}(G'_{30})^*\exp(i\mathbf{k}_S \cdot \mathbf{r})\exp(-i\omega_1 t)$.

With these expressions, the spatial periodic pattern formation of MWM signals can be investigated. It is clear that the periodical variation of singly-dressed FWM, doubly-dressed FWM and doubly-dressed SWM signals with respect to x -axis at $z = 0$, are all derived from the periodical dressing effects. With different probe detunings, these MWM signals will show profiles with significant differences. So, in order to analyze such dependence, we consider the so-called enhancement and suppression conditions due to dressing effect before investigating the MWM Talbot effects.

3 Suppression and Enhancement Conditions

The characteristics of FWM are affected by the dressing effect, which depends on Δ_1 , Δ_2 , and $|G_{2t}(x)|^2$. As shown in Fig. 2, because of $|G_{2t}(x)|^2$, $|1\rangle$ is split into two dressing states $|G_{2t}(x)\pm\rangle$ with eigen-frequencies $\lambda_{|G_{2t}(x)\pm\rangle} = \Delta_2/2 \pm \sqrt{\Delta_2^2/4 + |G_{2t}(x)|^2}$. Therefore, $|G_{2t}(x)\pm\rangle$ are periodic along x .

Absorption will be enhanced when the probe resonates with the dressing states, i.e., $\Delta_1 = -\lambda_{|G_{2t}(x)\pm\rangle}$, which corresponds to the electromagnetically induced absorption (EIA) condition. Accordingly, the FWM signal will get enhanced resonantly. Thus we define $\Delta_1 = -\lambda_{|G_{2t}(x)\pm\rangle}$ as the enhancement condition. While when the probe reaches two-photon resonance ($\Delta_1 + \Delta_2 = 0$), absorption will be suppressed (the EIT condition), and the FWM signal in such case will be suppressed correspondingly. Thus, we define $\Delta_1 + \Delta_2 = 0$ as the suppression condition. So, if Δ_1 is set at discrete values orderly from negative to positive and Δ_2 is scanned, we can obtain the periodic enhancement/suppression condition and FWM signals along x . In Figs. 2(a1)-(e1), we display the periodic FWM signals along x corresponding to different Δ_1 , and the insets are the dependence of the FWM signal intensity on Δ_2 at $z = 0$ and $x = 0$. In Figs. 2(a2)-(e2), we exhibit the corresponding split energy level diagrams, and in Figs. 2(a3)-(e3) the corresponding periodic properties of the split energy levels along x . In Fig. 2(a1), Δ_1 is relatively large and positive, and we only consider the enhancement because of the weakness of the suppression. When Δ_1 decreases but is still positive, Δ_2 will meet the enhancement condition ($\Delta_1 = -\lambda_{|G_{2t}(x)+\rangle}$) first, and then the suppression condition as shown in Fig. 2(b1). Because of $\Delta_1 = 0$ in Fig. 2(c1), so that Δ_2 can never meet the enhancement condition. The case in Fig. 2(d1) is opposite to that in Fig. 2(b1). And in Fig. 2(e1), the enhancement is dominant again, the same as that in Fig. 2(a1), for Δ_1 is relatively large and negative.

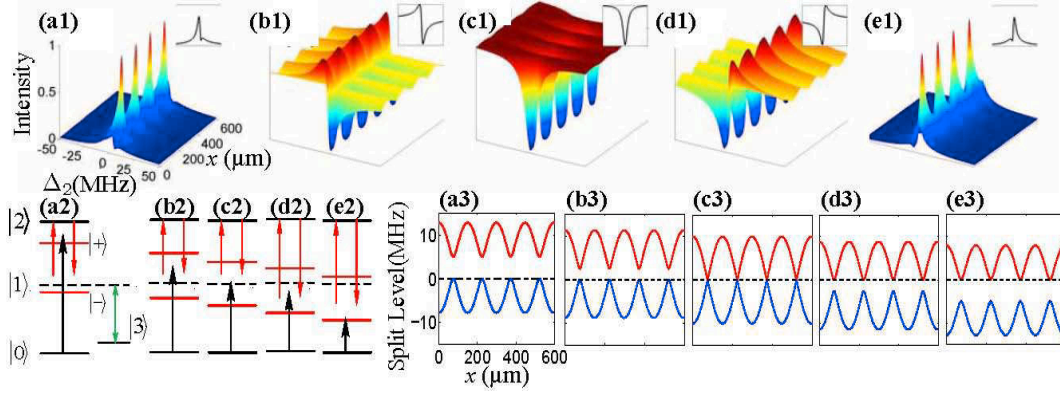


Figure 2: The normalized intensities versus Δ_2 and x of singly-dressed FWM with (a1) enhancement effect, (b1) enhancement-suppression effect, (c1) suppression effect, (d1) suppression-enhancement effect, and (e1) enhancement effect, corresponding to $\Delta_1 = -5$ MHz, -4 MHz, 0 , 4 MHz, and 5 MHz, respectively. The insets are the incident intensity versus Δ_2 . (a2)-(e2) The corresponding split energy level (red lines marked $|+\rangle$ and $|-\rangle$ on the right are split energy levels, the dotted line is the initial energy level) diagrams with dressing fields at $x = 0$. (a3)-(e3) The corresponding periodic split energy levels versus x . The other parameters are $G_2 = 15$ MHz, $\Gamma_{10} = 5$ MHz, and $\Gamma_{20} = 1$ kHz.

For the doubly-dressed MWM signals \mathbf{E}_{F2} and \mathbf{E}_S , we take \mathbf{E}_{F2} to execute our discussions. First, the interference between \mathbf{E}_3 and \mathbf{E}'_3 leads to periodic dressing effect, and therefore split the naked state into two dressing states $|G_{3t}(y)\pm\rangle$ with eigen-frequencies $\lambda_{|G_{3t}(y)\pm\rangle} = -\Delta_3/2 \pm \sqrt{\Delta_3^2/4 + |G_{3t}(y)|^2}$. \mathbf{E}_2 and \mathbf{E}'_2 also act as dressing fields, so the first-order dressing state $|G_{3t}(y)\pm\rangle$ will split into second-order dressing states $|G_{3t}(y) \pm G_{2t}(x)\pm\rangle$ with frequencies

$$\lambda_{|G_{3t}(y)-G_{2t}(x)\pm\rangle} = \frac{-\Delta_3 - \sqrt{\Delta_3^2/4 + |G_{3t}(y)|^2}}{2} + \frac{\Delta'_2 \pm \sqrt{\Delta_2'^2/4 + |G_{2t}(x)|^2}}{2}, \quad (9)$$

$$\lambda_{|G_{3t}(y)+G_{2t}(x)\pm\rangle} = \frac{-\Delta_3 + \sqrt{\Delta_3^2/4 + |G_{3t}(y)|^2}}{2} + \frac{\Delta''_2 \pm \sqrt{\Delta_2''^2/4 + |G_{2t}(x)|^2}}{2}, \quad (10)$$

where $\Delta'_2 = \Delta_2 - \{-\Delta_3 - \sqrt{\Delta_3^2/4 + |G_{3t}(y)|^2}\}/2$, $\Delta''_2 = \Delta_2 - \{-\Delta_3 + \sqrt{\Delta_3^2/4 + |G_{3t}(y)|^2}\}/2$, respectively.

Similar to the case for \mathbf{E}_{F1} , we can also investigate the enhancement and suppression for \mathbf{E}_{F2} and \mathbf{E}_S . And their enhancement and suppression correspond to $\Delta_1 = -\lambda_{|G_{3t}(y)\pm G_{2t}(x)\pm\rangle}$ and $\Delta_1 + \Delta_2 = 0$, respectively. The periodic doubly-dressed FWM signals along x corresponding to different conditions are shown by the mesh plots in Figs. 3(a1)-(i1) with insets being the dependence of the signal intensity on Δ_2 at $z = 0$ and $x = 0$. The corresponding split energy level schematics are shown in Figs. 3(a2)-(i2), and the corresponding spatial periodic energy levels in Figs. 3(a3)-(i3). Doubly-dressed SWM enhancement and suppression effects are similar to the results shown in Fig. 3. In light of the SWM here is a two dimensional (2D) case, we exhibit two cases of the second order splitting energy levels as shown in Figs. 4(a) and (b).

4 Talbot Effect of MWM Signals

In the perspective of Fourier optics, the transfer function of a Fresnel diffraction system with z as the propagation axis, can be expressed as $H_F(\xi) = \exp(ik_z z) \exp(-i\pi\lambda z \xi^2)$ in frequency domain [29], where ξ is the spatial frequency and k_z is the projection of \mathbf{k} along z . The field of the MWM signal $g_0(x, y) \propto \rho(x, y)$, so it can be expanded into two-dimension (2D) Fourier series as $g_0(x, y) = \sum_{m,n=-\infty}^{\infty} c_{m,n} \exp[i2\pi(n x/d_x + m y/d_y)]$, and in frequency domain the equation above can be written as

$$G_0(\xi, \eta) = \sum_{m,n=-\infty}^{\infty} c_{m,n} \delta\left(\xi - \frac{n}{d_x}\right) \cdot \delta\left(\eta - \frac{m}{d_y}\right), \quad (11)$$

where $c_{m,n}$ is the Fourier coefficient. So, considering the Fresnel diffraction, the MWM signal at a z distance is

$$G(\xi, \eta) = G_0(\xi, \eta) \exp(ik_z z) \exp[-i\pi\lambda_1 z (\xi^2 + \eta^2)]. \quad (12)$$

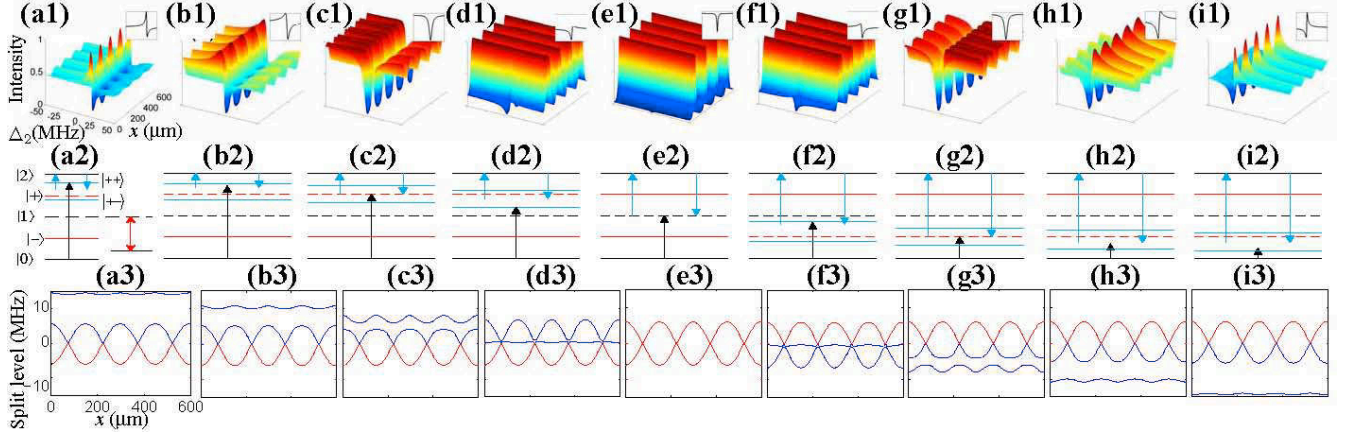


Figure 3: The normalized intensities versus Δ_2 and x of (a1) doubly-dressed FWM with enhancement effect, (b1) enhancement-suppression effect, (c1) suppression effect, (d1) suppression-enhancement effect, (e1) suppression effect, (f1) enhancement-suppression effect, (g1) suppression effect, (h1) suppression-enhancement effect, and (i1) enhancement effect, corresponding to $\Delta_1 = -18$ MHz, -8 MHz, -5 MHz, -2 MHz, 0 , 2 MHz, 5 MHz, 8 MHz, and 18 MHz, respectively. The insets are the incident intensity versus Δ_2 . (a2)-(i2) The corresponding split energy level diagrams with dressing fields at $x = 0$. (a3)-(i3) The corresponding periodic split energy levels versus x . The other parameters are $\Delta_3 = 0$, $G_2 = G_3 = 15$ MHz, $\Gamma_{10} = 5$ MHz, and $\Gamma_{20} = 1$ kHz.

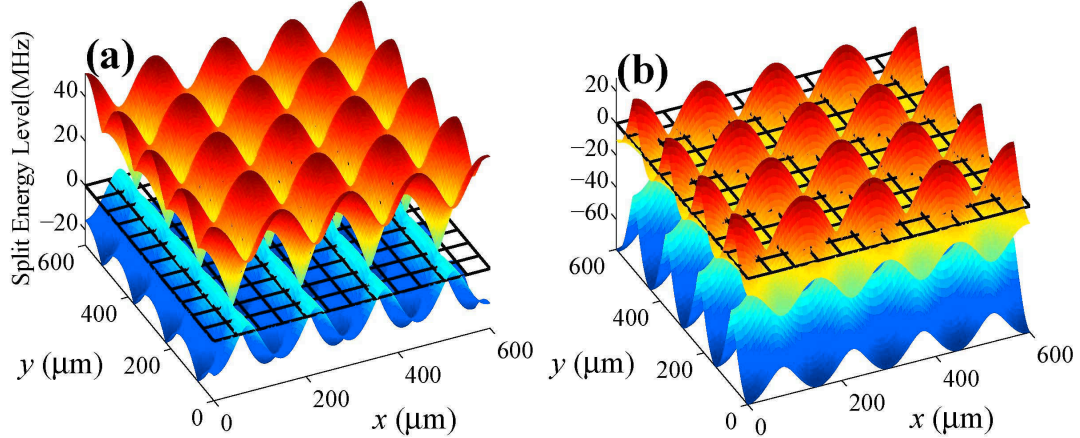


Figure 4: (a) The surfaces represent $|G_{3t}(y) + G_{2t}(x)+\rangle$ (top), $|1\rangle$ (grid), and $|G_{3t}(y) + G_{2t}(x)-\rangle$ (bottom), respectively. (b) The surfaces are $|G_{3t}(y) - G_{2t}(x)+\rangle$ (top), $|1\rangle$ (grid), and $|G_{3t}(y) - G_{2t}(x)-\rangle$ (bottom), respectively. $\Delta_2 = 2$ MHz for (a) and -2 MHz for (b). The values of the other parameters are $\Delta_3 = -3$ MHz, $G_{20} = G'_{20} = G_{30} = G'_{30} = 15$ MHz, $\Gamma_{10} = 5$ MHz, $\Gamma_{20} = \Gamma_{30} = 1$ kHz, $\lambda_1 = 776$ nm, $\lambda_2 = \lambda_3 = 780$ nm, $\theta_1 = \theta_2 = 0.3^\circ$.

Plugging Eq. (11) into Eq. (12), we end up with

$$G(\xi, \eta) = \sum_{m,n=-\infty}^{\infty} c_{m,n} \delta\left(\xi - \frac{n}{d_x}\right) \cdot \delta\left(\eta - \frac{m}{d_y}\right) \exp(ik_z z) \exp\left\{-i\pi\lambda_1 z \left[\left(\frac{n}{d_x}\right)^2 + \left(\frac{m}{d_y}\right)^2\right]\right\}. \quad (13)$$

For simplicity, we let $\lambda_2 = \lambda_3$ and $\theta_1 = \theta_2$, thus the periods along x and y are the same, i.e., $d_x = d_y$. Singly- and doubly-dressed FWM signals only concerns one SW formed by \mathbf{k}_2 and \mathbf{k}'_2 , and therefore we do not consider y component. In such a case, $\exp[-i\pi\lambda_1 z(n/d_x)^2] = 1$ if $z = 2qd_x^2/\lambda_1$ ($q = 1, 2, 3, \dots$), so after inverse Fourier transformation, we get

$$g(x) = g_0(x) \exp(ik_z z). \quad (14)$$

Because of $|g(x)|^2 = |g_0(x)|^2$, we can see the self-imaging of the MWM signals at $z = 2qd_x^2/\lambda_1$, and $z_T = z|_{q=1}$ is the Talbot length. It is worth mentioning that the images on the z_T/N planes are fractional Talbot images [30], where N is an integer bigger than 1.

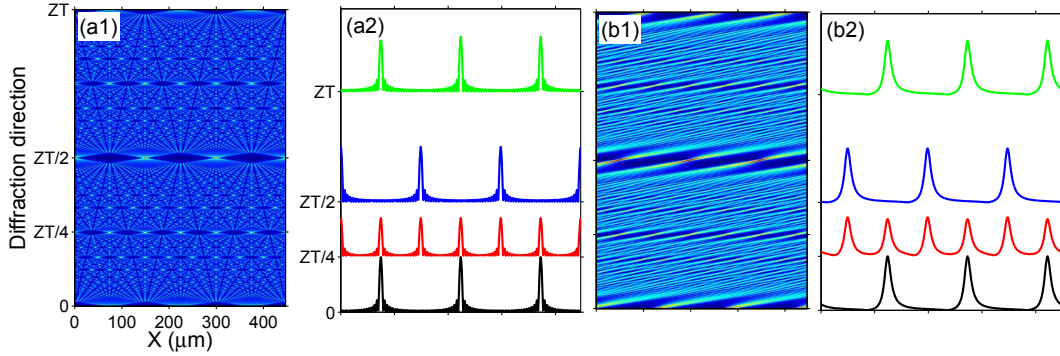


Figure 5: (a1) The Talbot effect carpets for \mathbf{E}_{F1} under suppression conditions with $\Delta_1 = 3$ MHz and $\Delta_2 = -3$ MHz. (b1) The Talbot effect carpets for \mathbf{E}_{F1} under enhancement conditions with $\Delta_2 = -3$ MHz and $-\Delta_1 = \Delta_2/2 + \sqrt{\Delta_2^2/4 + |G_{2t}(x)|^2}$. (a2) and (b2) The intensity profiles at $z = 0$ (black curves), $z = z_T/4$ (red curves), $z = z_T/2$ (blue curves), and $z = z_T$ (green curves), respectively. The other parameters are $G_{20} = G'_{20} = 15$ MHz, $\Gamma_{10} = 5$ MHz, and $\Gamma_{20} = \Gamma_{30} = 1$ kHz.

We firstly choose \mathbf{E}_{F1} as the incidence to execute the simulation. As shown in Fig. 2, the spatial profile of the incident signal varies along Δ_2 with different Δ_1 , and this variation leads to different diffraction process of FWM signal under different conditions. Figs. 5(a1) and (b1) are the corresponding Talbot effect carpets under suppression conditions and enhancement conditions, respectively. Figs. 5(a2) and (b2) are the intensity profiles of the repeated images cutted at certain fractional Talbot lengths. From Fig. 5, we can not only clearly see the periodic singly-dressed FWM can reappear along z , but also see that the carpet stripes are oblique and such obliquity is more obvious under enhancement conditions.

For \mathbf{E}_{F2} , the results are shown in Fig. 6. Clearly, we obtain the self-imaging of the incident \mathbf{E}_{F2} at the Talbot plane again, no matter it is under the suppression or the enhancement conditions. In contrary to the case in Fig. 5(a1), which is obtained under suppression conditions, the Talbot effect shown in Fig. 6(a1) seems oblique. Under enhancement conditions the carpet stripes are more obvious as shown in Fig. 6(b1), but the obliquity is almost the same with that shown in Fig. 6(a1). By comparing the Talbot carpets shown in Fig. 6(b1) and Fig. 5(b1), we find the obliquity and the width of the stripes are almost unchanged.

Last but not the least, we discuss the Talbot effect from \mathbf{E}_S . We consider two orthogonal SWs from two couple of dressing fields \mathbf{E}_2 , \mathbf{E}'_2 and \mathbf{E}_3 , \mathbf{E}'_3 simultaneously, to form a 2D lattice, which is periodic both along x and y as shown in Fig. 1(d), thus a 2D SWM signal will be excited. In Figs. 7 and 8, we first give the iso-surface plots of the Talbot effect of the 2D SWM signal under suppression conditions and enhancement conditions, respectively. And then we choose four intensity plots at certain places during propagation to show the details more clearly. We can see that at the Talbot length as shown in Figs. 7(d) and 8(d), the 2D SWM signals are reproduced. At half the Talbot length as shown in Figs. 7(c) and 8(c), the self-images shifted half period both along x and y . At one quarter of the Talbot length, fractional self-images can be seen as shown in Figs. 7(b) and 8(b), in which the images are twice as many as those in Figs. 7(a) and 8(a). Under enhancement conditions shown in Fig. 8, the images are more clear than those under suppression conditions as shown in Fig. 7. Here, we want to point out the reason that the periods of fractional Talbot effects shown in Figs. 5(b2), 6(a2) and (b2), and 8(b) seemingly not

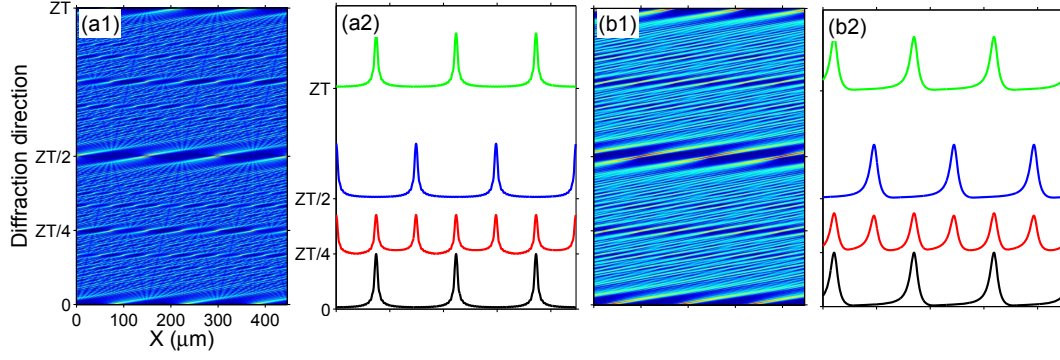


Figure 6: (a1) The Talbot effect carpets for \mathbf{E}_{F2} under suppression conditions with $\Delta_1 = 18$ MHz, $\Delta_2 = -18$ MHz, and $\Delta_3 = 18$ MHz. (b1) The Talbot effect carpets for \mathbf{E}_{F2} under enhancement conditions with $\Delta_2 = -18$ MHz, $\Delta_3 = 18$ MHz, and Δ_1 based on Eq. (9). (a2) and (b2) The setup is as Figs. 5(a2) and (b2). The other parameters are $G_{20} = G'_{20} = 15$ MHz, $G_{30} = 2$ MHz, $\Gamma_{10} = 5$ MHz, and $\Gamma_{20} = \Gamma_{30} = 1$ kHz.

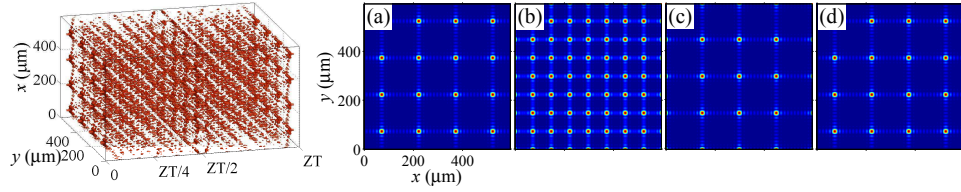


Figure 7: The iso-surface plot is the Talbot effect for \mathbf{E}_S under the suppression condition. The four panels are the contour plots of the Talbot effect at $z = 0$ (a), $z = z_T/4$ (b), $z = z_T/2$ (c), and $z = z_T$ (d), respectively. The parameters are $\Delta_1 = 18$ MHz, $\Delta_2 = -18$ MHz, $\Delta_3 = 18$ MHz, $G_{20} = G'_{20} = G_{30} = G'_{30} = 15$ MHz, $\Gamma_{10} = 5$ MHz, $\Gamma_{20} = \Gamma_{30} = 1$ kHz,

the half period at $z = 0$, is due to the inertial weakness of the numerical simulations. The Talbot effect changes dramatically during propagation, especially around small fractional Talbot lengths. Even a tiny deviation from the exact $z_T/4$ will bring seemingly imperfect quarter Talbot effect. Calculations with very high resolution will help us approach perfect fractional Talbot effects, but beyond our computer's memory.

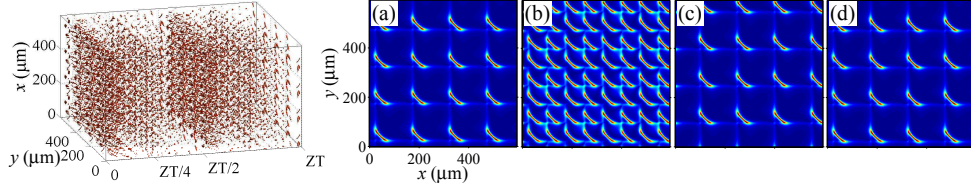


Figure 8: The Talbot effect for \mathbf{E}_S under the enhancement condition. The setup is as the Fig. 7, but with Δ_1 according to Eq. (10).

5 Conclusion

In conclusion, we have studied the Talbot effects with completely controllable MWM signals. We have obtained the spatially periodic FWM and SWM signals by the interference between two dressing fields in a reverse Y-type atomic level system. The intensities of the MWM signals can be effectively controlled via enhancement conditions and suppression conditions derived from dressing effect. Talbot effect from singly- as well as doubly-dressed FWM is observed in the numerical experiment. Different from the case of FWM, for SWM, we construct a 2D lattice, from which the SWM is 2D modulated, to investigate the 2D Talbot effect. We find that the numerical simulations agree with the theoretical predictions very well. Our scheme is more advantageous in the controllability, compared to the previous studies, mainly attributed to the modulation of the MWM signal by the dressing effect. Our findings

not only enrich the understanding of the MWM theory, but also offer a different method to investigate the Talbot effect.

Acknowledgement

This work was supported in part by the 973 Program 2012CB921804; by the NNSFC under Grants 10974151, 61078002, 61078020, 11104214, 61108017, and 11104216; by the NCET under Grant 08-0431; by the RFDP under Grants 20110201110006, 20110201120005, and 20100201120031; and by the FRFCU under Grants 2011JDHZ07, XJJ2011083, XJJ2011084, XJJ20100151, XJJ20100100, and XJJ2012080.

References

- [1] H. F. Talbot, “Facts relating to optical science,” *Philos. Mag.*, vol. 9, no. 56, pp. 401–407, 1836.
- [2] L. Rayleigh, “On copying diffraction-gratings, and on some phenomena connected therewith,” *Philos. Mag.*, vol. 11, no. 67, pp. 196–205, 1881.
- [3] K. Patorski, “The self-imaging phenomenon and its applications,” *Prog. Opt.*, vol. 27, pp. 1–108, 1989.
- [4] M. S. Chapman, C. R. Ekstrom, T. D. Hammond, J. Schmiedmayer, B. E. Tannian, S. Wehinger, and D. E. Pritchard, “Near-field imaging of atom diffraction gratings: The atomic Talbot effect,” *Phys. Rev. A*, vol. 51, no. 1, pp. R14–R17, 1995.
- [5] C. Ryu, M. F. Andersen, A. Vaziri, M. B. d’Arcy, J. M. Grossman, K. Helmerson, and W. D. Phillips, “High-order quantum resonances observed in a periodically kicked Bose-Einstein condensate,” *Phys. Rev. Lett.*, vol. 96, no. 16, p. 160403, 2006.
- [6] M. R. Dennis, N. I. Zheludev, and F. J. G. de Abajo, “The plasmon Talbot effect,” *Opt. Express*, vol. 15, no. 15, pp. 9692–9700, Jul 2007.
- [7] A. A. Maradudin and T. A. Leskova, “The Talbot effect for a surface plasmon polariton,” *New J. Phys.*, vol. 11, no. 3, p. 033004, 2009.
- [8] H. Müller-Ebhardt, H. Rehbein, C. Li, Y. Mino, K. Somiya, R. Schnabel, K. Danzmann, and Y. Chen, “Quantum-state preparation and macroscopic entanglement in gravitational-wave detectors,” *Phys. Rev. A*, vol. 80, no. 4, p. 043802, 2009.
- [9] R. Iwanow, D. A. May-Arrioja, D. N. Christodoulides, G. I. Stegeman, Y. Min, and W. Sohler, “Discrete Talbot effect in waveguide arrays,” *Phys. Rev. Lett.*, vol. 95, no. 5, p. 053902, 2005.
- [10] Y. Zhang, J. Wen, S. N. Zhu, and M. Xiao, “Nonlinear Talbot effect,” *Phys. Rev. Lett.*, vol. 104, no. 18, p. 183901, 2010.
- [11] J. Wen, Y. Zhang, S.-N. Zhu, and M. Xiao, “Theory of nonlinear Talbot effect,” *J. Opt. Soc. Am. B*, vol. 28, no. 2, pp. 275–280, 2011.
- [12] J. Wen, S. Du, H. Chen, and M. Xiao, “Electromagnetically induced Talbot effect,” *Appl. Phys. Lett.*, vol. 98, no. 8, p. 081108, 2011.
- [13] A. André and M. D. Lukin, “Manipulating light pulses via dynamically controlled photonic band gap,” *Phys. Rev. Lett.*, vol. 89, no. 14, p. 143602, 2002.
- [14] M. Artoni and G. C. La Rocca, “Optically tunable photonic stop bands in homogeneous absorbing media,” *Phys. Rev. Lett.*, vol. 96, no. 7, p. 073905, 2006.
- [15] J.-W. Gao, Y. Zhang, N. Ba, C.-L. Cui, and J.-H. Wu, “Dynamically induced double photonic bandgaps in the presence of spontaneously generated coherence,” *Opt. Lett.*, vol. 35, no. 5, pp. 709–711, 2010.
- [16] J.-H. Wu, M. Artoni, and G. C. L. Rocca, “Controlling the photonic band structure of optically driven cold atoms,” *J. Opt. Soc. Am. B*, vol. 25, no. 11, pp. 1840–1849, 2008.

- [17] A. Imamoglu and S. E. Harris, “Lasers without inversion: interference of dressed lifetime-broadened states,” *Opt. Lett.*, vol. 14, no. 24, pp. 1344–1346, 1989.
- [18] G. Wang, H. Lu, and X. Liu, “Dispersionless slow light in mim waveguide based on a plasmonic analogue of electromagnetically induced transparency,” *Opt. Express*, vol. 20, no. 19, pp. 20 902–20 907, 2012.
- [19] M. D. Lukin and A. Imamoglu, “Controlling photons using electromagnetically induced transparency,” *Nature*, vol. 413, no. 6853, pp. 273–276, 2001.
- [20] D. F. Phillips, A. Fleischhauer, A. Mair, R. L. Walsworth, and M. D. Lukin, “Storage of light in atomic vapor,” *Phys. Rev. Lett.*, vol. 86, no. 5, pp. 783–786, 2001.
- [21] C. Liu, Z. Dutton, C. Behroozi, and L. Hau, “Observation of coherent optical information storage in an atomic medium using halted light pulses,” *Nature*, vol. 409, no. 6819, pp. 490–493, 2001.
- [22] X. Liu, X. Yang, F. Lu, J. Ng, X. Zhou, and C. Lu, “Stable and uniform dual-wavelength erbium-doped fiber laser based on fiber bragg gratings and photonic crystal fiber,” *Opt. Express*, vol. 13, no. 1, pp. 142–147, 2005.
- [23] X.-M. Liu, “Theory and experiments for multiple four-wave-mixing processes with multifrequency pumps in optical fibers,” *Phys. Rev. A*, vol. 77, no. 4, p. 043818, 2008.
- [24] H. Ma and C. B. de Araújo, “Interference between third- and fifth-order polarizations in semiconductor doped glasses,” *Phys. Rev. Lett.*, vol. 71, no. 22, pp. 3649–3652, 1993.
- [25] B. Ham, P. Hemmer, and M. Shahriar, “Efficient electromagnetically induced transparency in a rare-earth doped crystal,” *Opt. Commun.*, vol. 144, no. 4–6, pp. 227–230, 1997.
- [26] J. Klein, F. Beil, and T. Halfmann, “Robust population transfer by stimulated raman adiabatic passage in a $\text{Pr}^{3+}:\text{Y}_2\text{SiO}_5$ crystal,” *Phys. Rev. Lett.*, vol. 99, no. 11, p. 113003, 2007.
- [27] H. Wang, A. Li, D. Du, Y. Fan, L. Wang, Z. Kang, Y. Jiang, J. Wu, and J. Gao, “All-optical routing by light storage in a $\text{Pr}^{3+}:\text{Y}_2\text{SiO}_5$ crystal,” *Appl. Phys. Lett.*, vol. 93, no. 22, p. 221112, 2008.
- [28] Y. Zhang and M. Xiao, *Multi-wave mixing processes: from ultrafast polarization beats to electromagnetically induced transparency*. Higher Education Press & Springer, 2009.
- [29] J. W. Goodman, *Introduction to Fourier Optics*, 3rd ed. Roberts and Company Publishers, 2005.
- [30] Z. Chen, D. Liu, Y. Zhang, J. Wen, S. N. Zhu, and M. Xiao, “Fractional second-harmonic Talbot effect,” *Opt. Lett.*, vol. 37, no. 4, pp. 689–691, 2012.